Bachelor of Science Thesis

Department of Physics

Particle and Nuclear Physics Division

Characterisation of the LYCCA Double-Sided Silicon Strip Detectors

---

Author
Marwan Mohamed
Supervisor
Pavel Golubev

LUND
UNIVERSITY

FYSK03 with a duration of 15 Hp
Examination
May 2023

Abstract

The goal of this thesis work is to describe the methods used and perform comprehensive testing of the Double-Sided Silicon-Strip Detectors (DSSD) prior to their implementation in the Lund-York-Cologne CAlorimeter (LYCCA) detector. In the framework of this project, the DSSD characterisation was carried out to ensure specification compliance prior to their "in-kind contribution" delivery to the HISPEC experiment at the NUSTAR collaboration. NUSTAR is one of the four scientific pillars of the future FAIR international accelerator facility currently under construction in Darmstadt, Germany. The main performance parameters obtained were the DSSD's operating voltage, strip-by-strip resolution, leakage current, etc. Two uncollimated alpha sources, ^{244}Cm and ^{148}Gd were used for the DSSD testing and performance studies. The energy spectra were measured by the dedicated real time data acquisition system. These spectra were analysed using a Python code to extract the detector's energy and position resolution. The DSSD's operation voltage and leakage current were obtained from the NIM module used for the detector's high voltage biasing. The intrinsic energy resolution was measured to be approx. 100 keV (FWHM) at 5.797 MeV. The measured resolution is higher than expected for this type of DSSD, which can be partially attributed to the electrical noise, non-uniformity of the dead layer thickness, and non-optimal FPGA-based digital signal processing algorithms.

Acknowledgments

I would like to thank my supervisor Pavel for being a great mentor, helping me understand my tasks and discussing with me the problems I have faced during this work. In addition to being easily available for me to contact and get in touch, that truly made this work more enjoyable than anticipated. I also want to thank Dr. Luis Sarmiento for helping me out with all the digital signal processing and analysis conducted using GO4 as well as answering every small insignificant question I had about the software. Special thanks to everyone in the nuclear structure group for making this period quite enjoyable and a pleasant working environment. Finally, I would like to extend my gratitude towards my family and friends who were there for me during every step and supported me through the stressful times.

Contents

List of Abbreviations

DSSD: Double-Sided Silicon-Strip Detector
LYCCA: Lund-York-Cologne CAlorimeter
NUSTAR: NUclear STructure, Astrophysics and Reactions
FAIR: Facility for Antiproton and Ion Research
HISPEC: High-resolution In-flight SPECtroscopy
SSB: Surface Barrier Detector
FWHM: Full Width at Half Maxima
VB: Valence Band
CB: Conduction Band
MCA: Multi Channel Analyser
ADC: Analog to Digital Converter
DSP: Digital Signal Processing
FPGA: Field Programmable Gate Array
CSP: Charge Sensitive Pre-Amplifier

1 Introduction

In this work the characterisation of the DSSDs modules will be discussed. This discussion covers the work done to obtain the technical specifications of the LYCCA detector modules for the NUclear STructure, Astrophysics and Reactions (NUSTAR) group at Lund University. The LYCCA modules will be used at the NUSTAR project at FAIR using High-resolution In-flight SPECtroscopy (HISPEC) infrastructure [1]. The specifications obtained and discussed in this work will be used as an input specification for the usage and optimisation for the detectors in experiments. Throughout this project a deeper understanding of the operational principles of the detectors was acquired as well as the electronic signal procession chain involved in the processing of the raw data.

The LYCCA DSSD modules being tested in this work are instrumentation equipment that are part of the HISPEC program in project FAIR. The purpose of LYCCA is to identify exotic nuclei by their physical properties, mainly their number of protons and neutrons A and number of protons Z. The nuclei are exotic due to their deviation from the valley of stability in the nuclidic chart.

2 Semiconductors

As there are four decay mechanisms for radioactive decay, different types of detectors and tools are needed to accurately measure and analyse them respectively. The decay mechanisms for radioactive decay are alpha-, beta-, and gamma decay as well as spontaneous fission. The decay of a nuclei occurs because of their instability. To gain more stability the nuclei decays into a more stable nuclei called the daughter nuclei through the aforementioned decay mechanisms. The main mechanism that this work relies on is alpha decay, which produces a helium nucleus often called an alpha particle. The interaction between the alpha particle and the matter it passes through will be discussed in the following section.

2.1 Charged Particle interaction with matter

As charged particles pass though a gas or condensed matter, they interact with the atomic electrons. This interaction has a probabilistic nature described by the cross section of the particle. The cross section of a beam of particles impinging on a target particle is given by:

$$\sigma(E) = \int d\Omega \left(\frac{d\sigma}{d\Omega} \right), \tag{1}$$

where $d\Omega$ represents a solid angle the particles scattered into, and $\frac{d\sigma}{d\Omega}$ is the general form of the differential cross section defined as:

$$\frac{d\sigma}{d\Omega}(E, \Omega) = \frac{1}{F} \frac{dN_s}{d\Omega}, \tag{2}$$

where F is the incident flux, and N_s is the average number of particles scattered per time. The underlying physics of interactions of such kind for charged particles will be discussed further in the next section.

2.1.1 Energy loss for charged particles

As charged particles move through matter, they lose some of their energy or change direction of propagation, through inelastic or elastic scattering, respectively. Charged particles are classified into two categories: charged leptons and heavy particles (heavier than an electron).

In elastic scattering the charged particle collides with the electrons in the medium and changes its direction. This is done while conserving the total energy. As such this type of interaction is not as frequent as inelastic collision. Inelastic collisions result in the loss of a fraction of the charged particle's kinetic energy. This fraction is transferred to the electrons in the medium which are either excited or ejected from the atoms if the energy is high enough. The rate of the energy loss per unit length is known as the stopping power of the medium and is described by the Bethe-Bloch formula for charged particles interacting with electrons of atoms in the material [2],

$$-\frac{dE}{dx} = \left(\frac{ze^2}{4\pi\epsilon_0}\right)^2 \frac{4\pi Z\rho N_A}{Am\nu^2}\left(ln(\frac{2m\nu^2}{I}) - ln(1-\beta^2) - \beta^2\right), \tag{3}$$

where ze is the ion's electronic charge, $\nu = \beta c$ is its velocity, m is the electron mass, N_A is Avogadro's number, while A, Z and ρ are the atomic mass number, atomic number and density of the stopping material respectively, and I is the mean ionization energy of an atom in the medium. The stopping power is both proportional to the charge of the charged particle squared, z^2, as well as the atomic number of the medium Z.

As the charged particle goes through the medium the rate of energy loss increases since the particle is losing energy. This increase in energy loss increases the number of ions produced in the medium in the particles path. As the particle reaches the end of its path, the rate of energy loss reaches a maximum known as the Bragg peak, after which it drops to zero as the particle comes to rest.

Electrons on the other hand deviate from the straight-line path due to their low mass and the electrical attraction to the nucleus, and radiate bremsstrahlung radiation. At small energies of a few MeV or less bremsstrahlung radiation is a relatively small factor, but as the energy increases it's probability of occurring increases. This leads to the loss of energy due to radiation being greater or equal to the collision-ionisation loss described before. Thus the total energy loss for electrons/positrons is comprised of two terms:

$$\frac{dE}{dx}_{tot} = \frac{dE}{dx}_{rad} + \frac{dE}{dx}_{colli}. \tag{4}$$

The $\frac{dE}{dx}_{coli}$ term is just the Bethe-Bloch formula but slightly modified due to the electron's small mass and that the collision is between two identical particles, while the $\frac{dE}{dx}_{rad}$ term is the radiation loss term.

2.1.2 Interaction of photons with matter

Photons on the other hand have different interaction mechanisms with matter since they do not have electrical charge. The three mechanisms are photoelectric effect, Compton scattering and pair production.

The photoelectric effect occurs when an electron absorbs a photon, resulting in the ejection of the electron from the atom it was bound to. The energy of the electron is:

$$E = h\frac{c}{\lambda} - I.E, \tag{5}$$

where h is Plank's constant, λ is the photon's wavelength, c is the speed of light, and $I.E$ is the energy required to ionise the atom. To achieve this effect the photon's energy need at be more than the I.E of the electron as the photoelectric cross section is higher at that energy.

On the contrary pair production requires a photon to have an energy of at least 1.022 MeV. That is because in pair production a photon is transformed into an electron and positron which have an energy rest mass of 511 keV each. Any excess energy above 1.022 MeV would be converted into the electron's and positron's kinetic energy.

Alternatively Compton scattering is when a photon collides with a free electron resulting in the photon scattering and the electron gaining energy. The electron is considered free if the photon's energy is high with respect to the electron's ionisation energy. As momentum and energy is conserved in this process one can obtain the scattering angle by the following equation:

$$cos(\theta) = 1 - \frac{m_e c}{h}(\lambda - \lambda_0), \tag{6}$$

where θ is the angle between the photon's previous direction of propagation and new direction, m_e is the mass of the electron, λ_0 is the wavelength of the photon before collision while λ is its wavelength after.

2.2 Conduction in solids

In this thesis the interaction of radiation with the detector material is of interest as such, it is important to understand the underlying physics of solid state detectors and their operational principles.

2.2.1 Silicon properties

The usage of semiconductor detectors for research in nuclear and particle physics has been increasing over the past few decades. One of the main materials used for detector manufacturing is silicon which is an intrinsic semiconductor. Semiconductors are crystal materials that exhibit an electron energy band structure. This structure is made of many discrete energy levels that are close to each other creating a continuum. The prohibited energy gaps are regions where there is no energy levels. The lowest energy band is called a valence band (VB) while the highest band is the conduction band (CB) and the prohibited energies between them are called the band gap as shown in Figure 1.

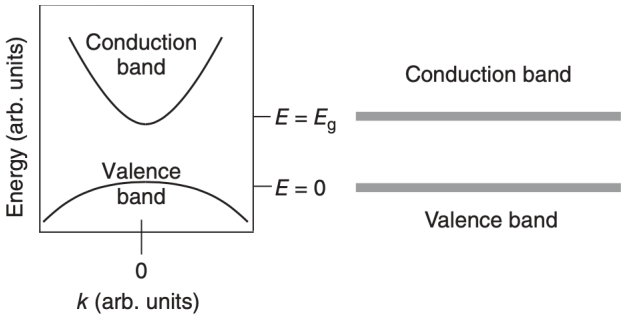

Figure 1: Figure showing the band structure of a semiconductor [3].

An intrinsic silicon semiconductor has a free electron concentration equal to that of the holes. This is achieved after the creation of electron-hole pairs due to thermal excitations. This equilibrium concentration is calculated using the following equation:

$$n_i = \sqrt{N_c N_v} exp(\frac{-E_g}{2kT}) = AT^{\frac{3}{2}} exp(\frac{-E_g}{2kT}), \tag{7}$$

where N_c is the number of of states in the conduction band, N_v the number of states in the valence band, k is the Boltzmann constant and E_g is the energy gap at 0 K. The electron-hole concentration is created due to thermal excitations at temperatures above 0 K. This is done by the excitation of a valence electron into the conduction band leaving a vacancy known as a hole in its position. In such configuration neighbouring valance electrons jump into the hole to fill it up. If such process is repeated, the hole is appearing to move through the semiconductor, which contributes to the common current though the valence band. The free electrons in the conduction band go through a similar process which contributes to the common current.

When an external electric field is applied to the semiconductor, the drift velocity of the charge carriers is described by:

$$\nu_e = \mu_e E, \nu_h = \mu_h E, \tag{8}$$

where μ is the mobility of the holes and electrons while E is the external electric field. The current density is described by $J = \rho\nu$ where ρ is $\rho = en_i$ in the semiconductor. As such the current density in a pure semiconductor is given by:

$$J = en_i(\mu_e + \mu_h)E. \tag{9}$$

2.2.2 Doping silicon

Doping a semiconductor leads to an increase in the current density, this is done by introducing impurities to the material. The impurities have a different number of valence electrons than the semiconductor, either one extra or deficient. When the dopant has a higher number of electrons which is called a donor an extra discrete energy level is created in the band gap close to the conduction band, in silicon this level is separated from the valence band by approximately 0.05 eV [4]. At temperatures above 0 K the extra electron is easily excited into the conduction band, thus increasing the electron concentration in

the conduction band. This leads to the current being predominantly due to the electron movement, called the majority charge carriers while the holes are called minority charge carriers. Having electrons as the majority charge carriers makes the semiconductor an n-type semiconductor.

Meanwhile a semiconductor with holes as the majority charge carriers is called a p-type semiconductor. This is due to the dopant material having less valence electrons than the semiconductor, often called an acceptor. This creates an extra discrete energy level in the band gap closer to the valence band. That allows the electrons in the valence band to thermally excite to this level, increasing the hole concentration making them the majority charge carriers, while the electrons are the minority charge carriers. The typical p-type dopant materials that are used are boron, aluminium and gallium. While n-type dopants material are phosphorous, arsenic and antimony.

For both n and p-type semiconductors the concentration of electrons (n) and holes (p) in thermal equilibrium obey the following equation:

$$np = n_i^2 = AT^3 exp(\frac{-E_g}{kT}). \tag{10}$$

2.2.3 PN diode

These two semiconductor types can be joined to make a pn-junction (diode). The formation of such junction creates a depletion region in the area where the two types are connected. This region is created by the diffusion of the electrons from the n-side into the p-side, while the holes diffuse from the p-side into the n-side. As they diffuse, they meet, resulting in recombination. Recombination creates the depletion region where there are immobile ionised donors and acceptors without the carriers. An electric field is thus created between the p- and n-side of the diode. This field is responsible for sweeping away any electron or hole created or entering the region. The depletion region width d is dependent on the concentration of the impurities, which is shown in the following equation in terms of resistivity ρ for silicon detectors [4]:

$$d = \begin{cases} 0.53(\rho_n(V_0 + V_B))^{1/2}\ \mu m \text{ n-type} \\ 0.32(\rho_p(V_0 + V_B))^{1/2}\ \mu m \text{ p-type,} \end{cases} \tag{11}$$

where V_0 is the contact voltage, V_B is the reverse bias voltage and ρ is the resistivity for the p- and n-side respectively. From equation (11) it is shown that as the bias voltage increases the depletion width increases, resulting in a higher detection area for the detector. The bias voltage applied is limited to a maximum value due to the resistance of the detector. If exceeded the junction will breakdown and begin conducting. Due to its electrical and spacial configuration the depletion region also has a capacitance which is described by the following equation:

$$C = \epsilon \frac{A}{d}, \tag{12}$$

where A is the area of the depletion region, and d its width.

In addition to having a capacitance, the pn-junction has a thermally induced leakage current that flows through it while biased. This current is equal to the difference between

the diffusion and drift currents:

$$I_{leakage} = I_{diffusion} - I_{drift} = I_0(E^{eV_B/K_BT} - 1), \tag{13}$$

where the diffusion current is due to the movement of the majority electrons from the n-side to the p-side if their energy is high enough to counter act the electric field. While the drift current is due to the minority electrons from the p-side entering into the depletion region and being pulled into the n-side by the electric field.

In addition to the movement of minority carriers the leakage current is due to other sources. Such as thermally produced electron-hole pairs and surface channels. Surface channels is when the surface has some degree of n- or p-typeness; which is a conducting layer [5]. This is a complicated effect as it depends on many factors such as surface chemistry, contaminants, surrounding surface and the mounting type. The leakage current is a main contributor to the noise of the detector, setting a limit on the smallest signal pulse height that is possible to observe by the front-end readout electronics.

2.3 Geometries for silicon detectors

Silicon detectors come in many different geometries and forms but the main geometries that are of importance to this work are surface barrier detectors (SSB) and micro-strip detectors, which will be discussed below.

2.3.1 Surface Barrier detectors (SSB)

This type of detector is the most common used silicon detector for charged particle experiments. They are created by forming a junction between silicon and a metal, either n-type silicon with gold or p-type silicon with aluminium, which creates a quite similar junction in characteristics as a pn-junction. The junction created is called a Schottky barrier.

The detector is made by etching the surface of the silicon (n-type) in room temperature and then depositing a thin layer of gold by evaporation. The junction is then installed in an insulating ring where there are metallised surfaces for electrical contact, as shown in the Figure 2.

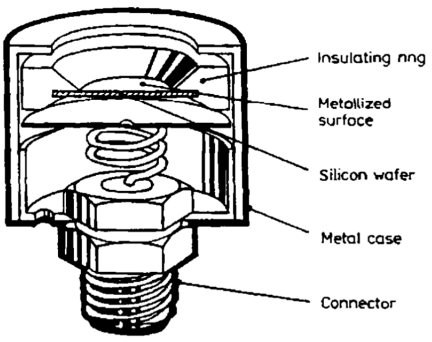

Figure 2: Figure showing the structure of an SSB detector [4].

Since the dead layer of the SSB can be as this as 1400 Å [6], a full depletion width is possible, leading to a better measurement of energy deposition of charged particles.

On the other hand they are very sensitive to light, due to the thin gold covering being insufficient to stop ambient light. They are also more susceptible to surface contamination and damage.

2.3.2 Micro-strip detectors

Micro-strip detectors have gained significant attention in nuclear and high energy physics. The reason is that it is made out of several readout strips placed about 20 μm apart, as shown in the Figure 3. In addition they have the ability of measuring both the position and energy of charged particles.

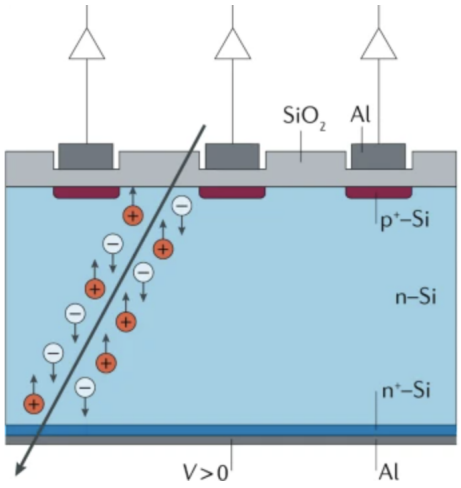

Figure 3: Figure showing the structure of a micro-strip detector [7].

As shown in Figure 3 the base material used is high resistivity n-type silicon and on top of it are p^+ diode strips with aluminium contacts for signal readout. These strips are ion beam implanted into the silicon creating pn-junctions at each strip-base contact. This side of the detector is called the p-side (or junction side) , while the n-side (or ohmic side) is the side where there is an n^+ electrode implanted into the silicon. Due to the thickness and wafer resistivity of such detectors, full depletion widths can be typically obtained with a bias voltage between 50 V and 100 V. Hence a fast response time is obtained which is needed in triggering devices in high energy physics. A more sophisticated type of detector that builds on this principle is the Double-Sided Silicon-Strip Detector or DSSD for short. This detector has strips on both the p- and n-side, providing spacial resolution as well. One side has the strips running down horizontally while the other has the strips vertically aligned.

3 Silicon Detectors

3.1 Signal formation in silicon sensors

When ionising radiation hits the detector, electron-hole pairs are created. If the radiation has an energy of E then $N_{e-h} = \frac{E}{w}$ electron-hole pairs should be ideally created, where w is the average energy required for ionisation in the detector, and E is the fully deposited energy. As the ionisation energy is absorbed, a certain number of electrons N_e are excited from the VB to CB, leaving an equal number of holes N_h in the VB. The applied voltage

drives the electrons and holes towards the electrodes of the detector where they are collected. The collection of charge Q at the electrodes depends on the efficiency n, leading to $Q = nJ = n\frac{E}{w}$. As such the voltage observed at the electrodes is:

$$V = \frac{Q}{C} = n\frac{N_{e-h}}{C} = n\frac{E}{wC}, \tag{14}$$

From equation (14) the voltage observed from the detector is linear to the number of electron-hole pairs created N_{e-h}. It is important to note that the energy required for the creation of electron-hole pairs is material and temperature dependent. For Silicon at 300 K the energy required is about 3.62 eV [4]. If the depletion region is smaller than the range of the incident particles only a fraction of the energy of the particles is deposited into the detector, resulting in a non-linear response. The depletion region also needs to be sufficiently thick such that the signals produced are larger than the noise level mostly set by the leakage current.

The signal that is observed at the electrodes is due to the induction created by the moving charges and not from the collection of charges. This signal takes time to go from zero to a maximum value. This is called rise time which is highly affected by the collection time and charge carriers mobility. The collection time is the time needed for the charge carriers to travel from their position to the electrodes.

After the generation of the signal, it is sent to a Charge Sensitive Pre-amplifier (CSP) since the capacitance of the detector is temperature dependent. The resolution of a detector can be extracted from the signal since similar to the voltage in equation (14) it is dependent on N_{e-h} and thus the energy E:

$$R = 2.35\frac{\sqrt{N_{e-h}}}{N_{e-h}} = 2.35\sqrt{\frac{w}{E}}, \tag{15}$$

where the factor 2.35 relates the standard deviation of a Guassian to its Full Width at Half Maxima (FWHM), which can also be used to calculate the resolution:

$$R_{FWHM} = \frac{FWHM}{E}. \tag{16}$$

3.1.1 Radiation damage

When radiation particles collides with dislocations in the detector's lattice, point defects are created, which is realised by the shifting of the atoms from their positions. As these defects are reoccurring they produce discrete trapping levels in the band gap, which increases the generation of electron-hole pairs by thermal excitations. This damage can be seen by an increase in the leakage current and a loss in resolution. Given that the damage is not significant the bias voltage can be increased to atone the resolution loss by decreasing the collection time. The radiation damage can also be recovered by thermo-annealing in most cases.

3.2 Conduction in solids

3.2.1 Front-end electronics

There are a couple of crucial components that need to be used to obtain the desired detector signal and extract spectroscopy information. These components are essential for

nuclear physics experiments and as such it is important to understand how they work.

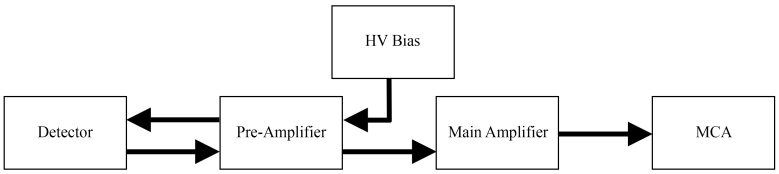

Figure 4: Figure showing the electronic components used in a nuclear physics experiment.

In Figure 4 the components needed to obtain the desired information and signal are shown. These components will be discussed in the following sections.

3.2.2 Charge sensitive pre-amplifier & amplifier

As mentioned before the signal observed at the electrodes is fed into a CSP. The purpose of the CSP is to convert the charge obtained from the detector into a signal and send it to the main amplifier. It is mounted as close as possible to the detector to minimise cable capacitance and inductance thus reducing the signal to noise ratio. Being charge sensitive, the pre-amplifier produces a voltage that is independent on the capacitance of the detector and linearly proportional to the depositied energy. Instead it depends on the CSP's feedback capacitance C_f, as shown in Figure 5.

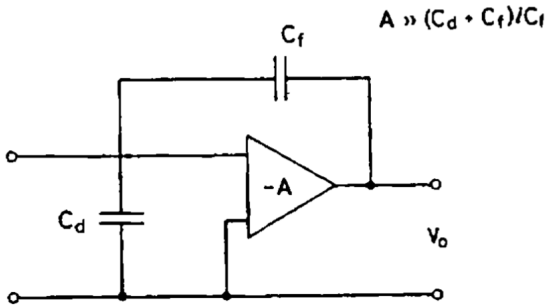

Figure 5: Figure showing the circuit of the pre-amplifier [4].

From Figure 5 one can deduce that the output voltage V_o is inversely proportional to the capacitance C_f.

$$V_o \approx -\frac{Q}{C_f}, \tag{17}$$

where Q is the charge collected in the capacitor. This charge needs to leave the capacitor, which is done through a slow discharge, producing the exponential tail pulse shown in Figure 6a, which has a characteristic time constant τ lasting between a few μs to 100 μs.

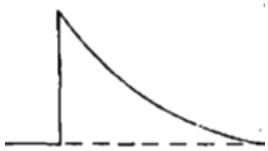

(a) Exponential tail pulse from the pre-amp.

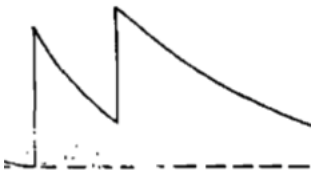

(b) Pulse Pile up from pre-amp.

Figure 6: Pulses obtained from pre-amp [4].

If a follow up signal arrives within the decay constant τ period, pulse pile up occurs as shown in Figure 6b. This pileup increases the amplitude of the signal, thus distorting the energy information as its proportional to the amplitude of the signal as shown in equation (14). To avoid such events a main amplifier is used to reshape the signal to a Gaussian form and amplify it. Reshaping the signal is done through either RC integration-differentiation and delay line shaping methods. Combinations of these circuits are used to improve signal-to-noise ratio which shapes the signal, as well as filter out RF disruptions and pole-zero correction.

3.2.3 Shaping

The most used method for pulse shaping is CR-RC pulse shaping [4]. This method relies on having the having the output of a CR circuit connected to the input of an RC circuit which results in the filtering of the pulse at low frequencies (differentiation) and high frequencies (integration) respectively. This leads to a better signal-to-noise ratio and produces a pulse, as shown in Figure 7.

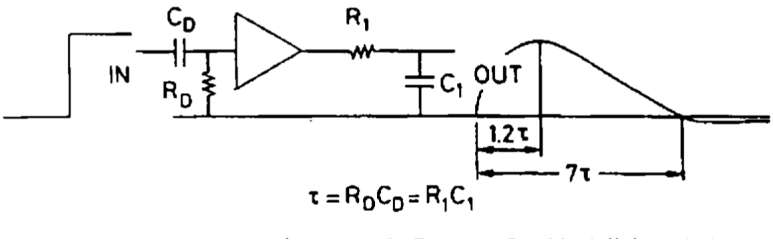

Figure 7: Figure showing the circuit of CR-RC circuits and its output [4].

The pulse produced by the CR-RC circuit shown in Figure 7 typically has an undershoot in it. As it can be seen more clearly in the Figure 8.

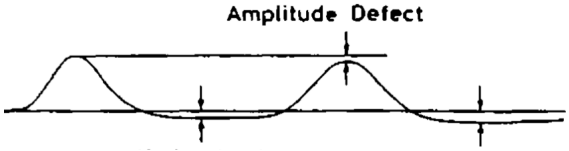

Figure 8: Figure showing the pulse generated from a CR-RC circuit [4].

Figure 8 shows the case when a second signal arrives and the overshoot is present. This creates a defect in the amplitude of the second pulse which is a problem. To fix it, a pole-zero cancellation circuit is connected to the CR part of the circuit. The circuit consists

of a variable resistor, which is changed until the undershoot vanishes when looking at the signal on an oscilloscope.

After the cancellation, an undershoot might still occur due to differentiations that happen after it because of the output circuitry of the amplifier. To decrease such effect the output capacitor has a larger time constant than the signal. Which is perfect for low count rates, but problematic for higher ones, as the pulses start to fall on top of each other leading to the multiplication of the undershoot and baseline shift. Baseline resorting circuits are placed at the output of the amplifier to fix this issue, by shorting the capacitor to ground after a pulse passes as a means of shortening the long decay time of the undershoot.

Another way of avoiding the baseline shift at high count rates is the usage of CR-RC-CR shaping circuits. These circuits create a bipolar pulse compared to the uni-polar pulse created by CR-RC circuits.

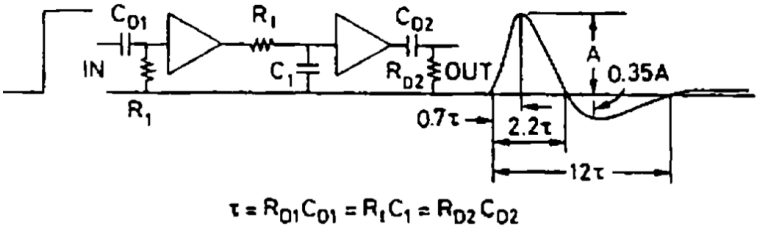

Figure 9: Figure showing a CR-RC-CR and the pulse it generates [4].

When a bipolar pulse shown in Figure 9 passes through the capacitor it leaves no residual charge unlike the uni-polar pulse, bypassing the baseline shifts that occur. The bipolar pulse is mainly used for high count rates as it produces a better resolution, but for lower count rates uni-polar pulses are used as they have a better signal-to-noise ratio.

3.2.4 MCA

The last but not least instrumentation needed after the amplifier is the multichannel analyser (MCA). This device extracts pulse information such as their heights (amplitudes) and keeps track of the number of times that height has been registered in a multichannel memory. The amplitudes of the pulses are first digitized by an analog-to-digital converter (ADC), and then assigned a memory channel to that digitised value. The amount of channels an MCA can digitise the amplitudes in is known as the conversion gain, and this can range from 128 to 16k depending on the specific experimental setup. In this work a peak sensitive ADC was used.

3.2.5 ADC

Digitisation of the pulse is handled by the ADC as mentioned before. The basic principle behind it is that it converts an analog signal of certain voltage V (amplitude) into a digital number (binary). There are many techniques available, one of the most used for spectroscopy ADC's is the Wilkinson method [8, 4]. The input signal - which is analog - charges a capacitor, which is discharged at a constant rate. As soon as it starts discharging a scaler is gated on. The scaler counts the pulses from an oscillator or clock with a constant frequency. The number of counts obtained in the scaler is proportional to the

charge in the capacitor.

Another digitisation technique that is widely used is the successive approximation method [9]. In this method the input pulse is compared to a range of reference voltages to evaluate its height. First a reference point is chosen and if the signal is higher or lower half of that reference point is added or subtracted to create a new reference point. The pulse height is then compared to this new reference point and the process continues in this manner until the pulse's height is known. The time taken for both of those digitisation techniques is called the conversion time, which has a value of around several tens of μs. This number varies as it depends on how many digits are desired. The successive approximation method is considered faster than the Wilkinson method but it is less linear, making the Wilkinson method more appropriate for spectroscopy work as stated before.

The linearity/non-linearity of the ADC is of importance as it can distort the spectrum's shape. The integral non-linearity is the deviation from the linear relation between the pulse height and the channel number. While the differential non-linearity is the inconstancy of the width of the individual channels.

4 Digital Signal Processing (DSP) and Analysis

In modern physics experiments the signal processing described in the previous sections i.e the shaping, pole-zero cancellation, and baseline restoration are all done digitally in a Field Programmable Gate Array (FPGA) integrated circuit [10]. This circuit takes the signals directly from the CSP, digitises it using an ADC and then using special algorithms shapes the pulse. The pulse is then sent to a peak detection block where the peak amplitudes are recorded. This entire process is controlled by an ARM processor [11] which then sends out the data stream to the computer for storage. The process can be described by the block diagram in Figure 10.

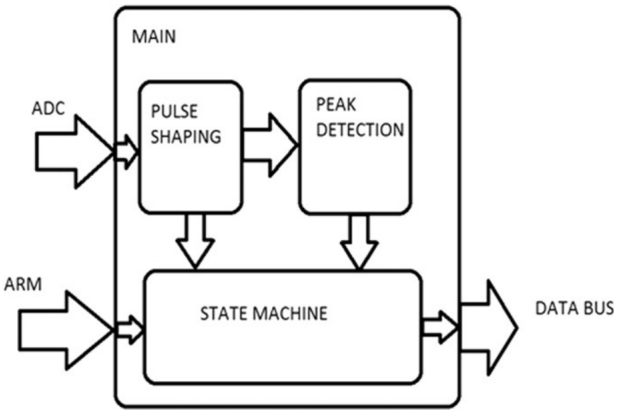

Figure 10: Figure showing the FPGA's process [10].

The detailed working of the peak detection and pulse shaping algorithms will not be discussed in this work as it is beyond it's scope. After the data stream is sent to the computer through the data bus, the peak amplitudes are saved in the memory channels using software called GO4 that is the digital equivalent to an MCA. DSP was used in this

work to perform multiparameter test of the LYCCA DSSDs as well as production of 2D and pn-strip hit patterns.

5 Procedure

5.1 Surface Barrier Detector

First the SSB detector was used to study all the properties of the detector and front-end electronics that were discussed in the sections before. The detector was mounted in a vacuum chamber where an Amptek A250CF CoolFET CSP was connected to it [12]. An oscilloscope was connected to the CSP's energy output for visual inspection of the signal from the detector. A ^{244}Cm sample was then placed at the height of the detector in the middle of the chamber. The chamber was pumped, to create a vacuum of (1.89 ± 0.04) mbar, after which the CSP and the detector were biased with (50.0 ± 0.1) V using the Mesytec MHV-4 supply unit. After which the Ortec 572A Amplifier was connected to the CSP instead and the signal was observed with the oscilloscope. The pole-zero cancellation was then adjusted until the undershoot was resolved, while setting the shaping time to be 2.5 μs and amplification of 200.

The Amp-shaper output was connected to the Ortec EASY-MCA 8k, to collect ^{244}Cm's spectrum, using Ortec's proprietary software MAESTRO [13]. After the collection of the spectrum, ^{244}Cm's was replaced by ^{148}Gd and a spectrum was collected with the same settings.

The bias voltage was then changed to values between (10.0 ± 0.1) V and (88.0 ± 0.1) V, to investigate how peak position changes and therefore charge collection efficiency with the bias voltage as shown in Figure 11a. This was done while having the same shaping time of 2.5 μs and amplification value of 200. To investigate how the shaping time affects detector resolution, the bias voltage was returned back to (50.1 ± 0.1) V. Then the shaping time was varied between 1 μs and 10 μs, with an amplification of 200. All these spectra were then imported into a Python code where it fits Gaussians to each peak after calibration and prints outs the amplitude, energy of peak, its resolution as well as graphs showing the relation between both peak position and bias voltage (Figure 11a), and resolution and shaping time (Figure 11b).

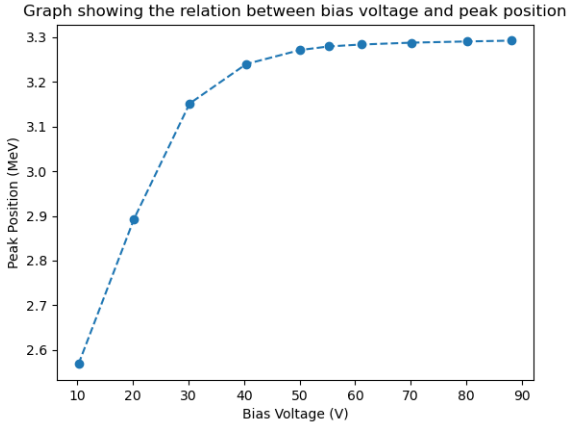

(a) Voltage vs peak position.

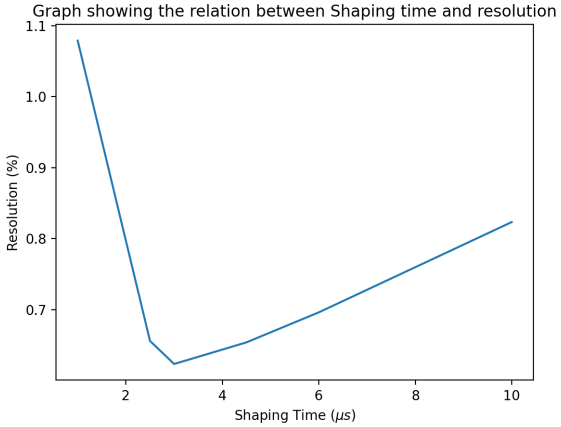

(b) Shaping time vs resolution of surface barrier detector.

Figure 11: Properties of surface barrier detectors.

Based on the data in Figure 11b the optimal shaping time is 2.9 μs. The last property to check was the detector readout chain linearity, which was done by first disconnecting all the electronics except the CSP and removing the radiation sources. The Ortec 419 Precision Pulse Generator was then connected to the CSP test input, while having both the energy output of the CSP and the pulse generator connected to the oscilloscope. The heights of both pulses was then recorded to be subsequently manipulated by the code to produce Figure 12.

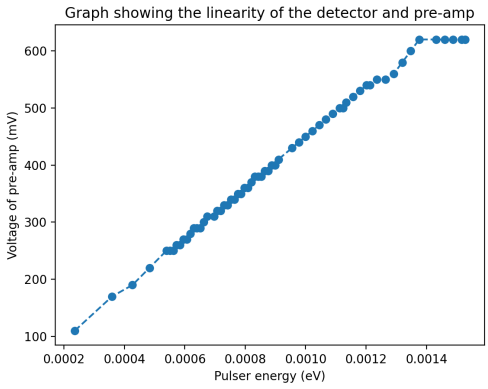

Figure 12: Linearity of detector.

5.2 Double-sided Silicon-Strip Detector Testing

The first DSSD module was first placed in a vacuum chamber, which is different than the one used for the SSB as shown in Figure 13a.

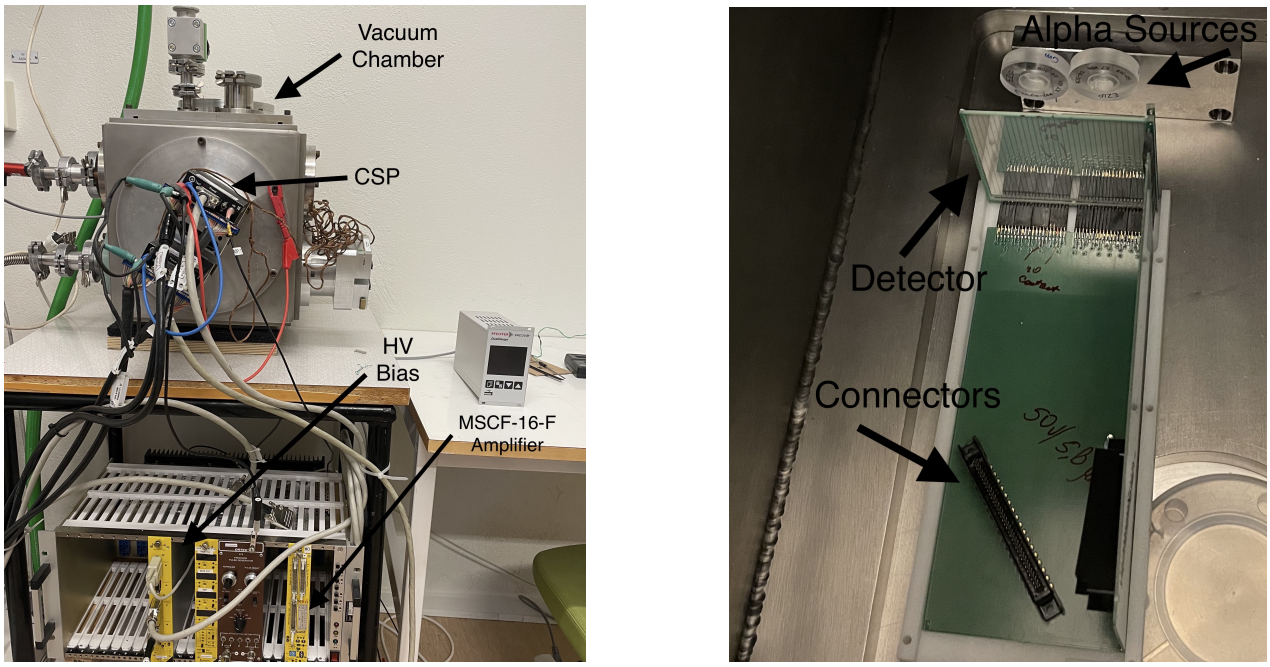

(a) Vacuum chamber of the DSSD.

(b) DSSD inside chamber

Figure 13: Experimental Setup

The module was then carefully connected to the chambers vacuum feed-through, which has the CSP mounted to it on the outside as shown in Figure 13a. The CSP was then connected to the Mesytec MSCF-16-F 16 channel amplifier so the signal can be observed using an oscilloscope. Both the ^{148}Gd and ^{244}Cm sources were then placed in the chamber, which was pumped afterwards to value of (1.89 ± 0.04) mbar. A bias voltage of (50.0 ± 0.1) V was then applied using the Mesytec MNV-4 supply unit and a signal was observed for each channel on the oscilloscope. This was then applied for all the remaining 48 channels of the detector, as it has 32 strips on both the n- and p-side.

After visual checking each channel and its signal, the four outputs of the CSP were then connected to four FPGA FEBEX 3 cards. Each card corresponded to 16 channels. Data was collected with a mask in front of the detector to investigate whether the mapping done in the code was correct. After that was accomplished and the mapping was corrected another set of data was collected without the mask. This was then done for all other five modules, with a bias voltage of (50.0 ± 0.1) V, while recording both leakage current and the room's temperature. This data was then unpacked using GO4's analysis tools and produced the individual spectrum of each strip. These spectra were then imported into a Python code that calibrated them, relating the channels to energy, using the following linear relation,

$$f(x) = ax + b, \tag{18}$$

where $f(x)$ is the energy, x is the channel number, a and b are the calibration variables. The peaks in the calibrated spectra are then fitted using Gaussians of the form,

$$f(x) = ae^{\frac{-(x-b)^2}{2c^2}}, \tag{19}$$

where b is the peak position, a is it's amplitude, and c is the standard deviation which is related to the FWHM by the factor 2.35. After obtaining the data the Python script

produced a file per detector containing the peak amplitude, energy, resolution and the calibration variables for each strip.

6 Results

The hit patterns produced by GO4's analysis tools are presented below for module 1. Figure 14a shows the hit pattern in terms of each strips while Figure 14b shows the 2D hit pattern. The resolution of each strip on both the p- and n-side can be seen in Figures 15a and 15b, respectively. The remaining modules and their respective hit patterns and resolution data can be found in Appendix 9.2 and 9.3 respectively along side the tables for the resolutions in Appendix 9.4. On the other hand one can see the average resolution in keV per module in Tables 2 and 3 as well as operating voltage and leakage currents in Table 1.

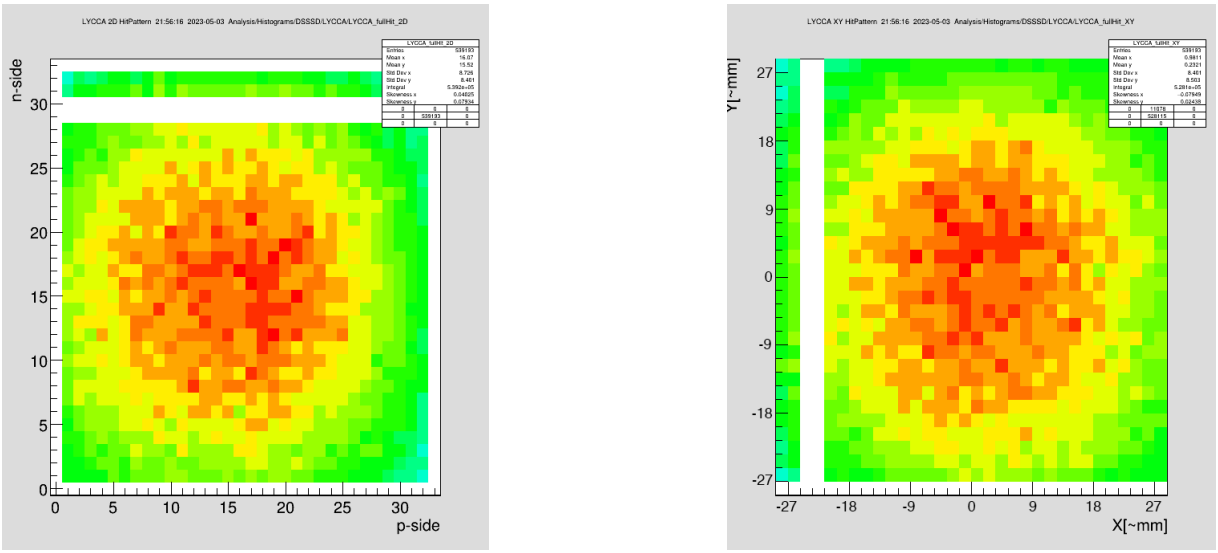

(a) PN pattern

(b) XY pattern

Figure 14: Module 1 hit patterns

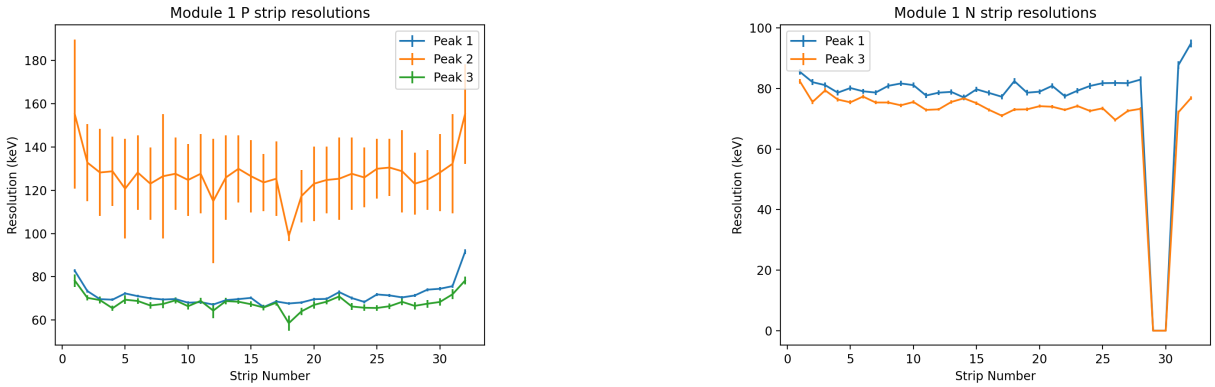

(a) P side resolution

(b) N side resolution

Figure 15: Module 1 resolutions, where any resolution value of 0 indicates that the strip is malfunctioning

Module No.	Voltage (V)	Current (μA)	Temp (C)
1	50.0 ± 0.1	0.169 ± 0.004	28 ± 1
2	50.0 ± 0.1	0.390 ± 0.001	28 ± 1
3	50.0 ± 0.1	0.487 ± 0.003	28 ± 1
4	50.0 ± 0.1	0.263 ± 0.001	27 ± 1
5	50.0 ± 0.1	3.300 ± 0.001	28 ± 1
6	50.0 ± 0.1	7.170 ± 0.001	28 ± 1

Table 1: Voltage and leakage current of each module at the room's temperature.

Module No.	Average Resolution (keV)		
	Peak 1 at 3.271 MeV	Peak 2 at 5.755 MeV	Peak 3 at 5.797 MeV
1	71.32 ± 0.12	127.1 ± 3.3	68.01 ± 0.32
2	90.80 ± 0.14	N/A	94.74 ± 0.07
3	111.73 ± 0.12	165.0 ± 0.7	78.08 ± 0.28
4	73.31 ± 0.12	N/A	84.87 ± 0.13
5	83.26 ± 0.11	N/A	99.72 ± 0.19
6	102.15 ± 0.14	116.0 ± 1.0	69.83 ± 0.25

Table 2: Average resolution of P side strips for all modules.

Module No.	Average Resolution (keV)	
	Peak 1 at 3.271 MeV	Peak 3 at 5.797 MeV
1	75.80 ± 0.16	69.88 ± 0.10
2	250.9 ± 0.7	202.05 ± 0.10
3	285.7 ± 0.8	223.95 ± 0.23
4	73.08 ± 0.18	79.79 ± 0.13
5	86.90 ± 0.20	86.83 ± 0.12
6	86.52 ± 0.18	91.47 ± 0.16

Table 3: Average resolution of N side strips for all modules.

7 Discussion

As it can be seen in Tables 2 and 3 the average resolution measured at FWHM of each module are around 100 keV at the energy of 5.797 MeV, which is considerably greater than the expected resolution for silicon detectors of around 18 keV [4]. A reason for such low resolution might be attributed to the instrumentation used, like the CSP as well as the FPGA performance and uncollimated alpha sources. The PFGA was most likely the cause of this behaviour as it produced a considerable amount of noise, which lead to the increase of the threshold used to trigger the data acquisition system.

The resolution trend with the increase of energy can not be observed as shown in Tables 2 and 3. This is not a significant issue as these detector modules will be used for particles with energies in the GeV range compared to the energies used in this work. It

is important to note that modules 2, 4 and 5 did not show the first alpha peak for ^{244}Cm on the p-side. This is due to the fact that ^{244}Cm's alpha spectra has two peaks which are relatively close in energy 5.755 MeV and 5.797 MeV to be exact [14]. This causes the peaks to overlap as shown in Figure 16 and depending on the detector's resolution they might be unresolvable. This was also the case for all n-side strips which is not a problem as they are considered less important than p-side strips.

Looking at Tables 4 through 15 it can be seen that some strips are not working, meaning that they will need to be examined for loose electrical bonding and fixing. While these individual strips will be fixed, the high leakage currents of modules 5 and 6 in Table 1 do suggest that they need to be annealed as they exceed the limit of 2 μA [15]. An interesting behaviour was spotted for the 26th n-side strip in the 4th module, where the peaks of both ^{244}Cm and ^{148}Gd where generated twice as shown in Figure 17.

This behaviour can be explained by improper positioning of the bonding contact of this strip. This positioning made it possible for the contact to touch the edge of the detector which is disconnected. As the edges of the detector are cut with a laser the electronic structure of the lattice in that site is altered resulting in defects in the lattice [16]. These defects can result in the change of the energy that the detector observe, thus shifting the peak's energy. Since both double peaks have relatively the same amplitude this leads to the conclusion that when an alpha particle hit that strip, the signals of both the strip and the edge of the detector were recorded. This conclusion is heavily supported by the fact that when the data were unpacked again by GO4, one can see both double peaks grow at the same rate. This behaviour eliminates the possibility that the data acquisition system might have malfunctioned during data collection.

8 Outlook and Conclusion

Overall the six modules tested do need further examination to fix the broken strips, and the possible annealing of modules 5 and 6 due to their high leakage current. The annealing process will result in the reorganisation of the atoms of the detectors which would fix any lattice defects contributing to the high leakage current. Further testing and analysis might be of interest to extract the pixel by pixel resolution which would be more accurate than the strip resolution obtained in this work. The reason for the higher accuracy is because the pixel by pixel resolution relates both a single p- and n-strip to each other. In addition the dead layer thickness can be found with the additional testing, resulting in a better understanding of the detectors' properties. After all the required repairs are done, the modules would be fit for experimental use in project FAIR. Where they will be used for the detection of heavy particle by their mass A and charge Z. In the duration of this work a testing setup was commissioned including software and hardware instrumentation for the testing of silicon detectors. As such this setup can be used again for the characterization of other silicon detectors in an efficient manner.

References

[1] P. Golubev et al. "The Lund–York–Cologne Calorimeter (LYCCA): Concept, design and prototype developments for a FAIR-NUSTAR detector system to discriminate relativistic heavy-ion reaction products". In: *Nuclear Instruments and Methods in Physics Research Section A: Accelerators, Spectrometers, Detectors and Associated Equipment* 723 (2013), pp. 55–66. ISSN: 0168-9002. DOI: https://doi.org/10.1016/j.nima.2013.04.058. URL: https://www.sciencedirect.com/science/article/pii/S0168900213004798.

[2] J. Lilly. *Nuclear Physics: Principles and Applications*. Wiley-VCH, 2001. ISBN: 978-0-471-97936-4. URL: https://books.google.se/books/about/Nuclear_Physics.html?id=agRC1r0qzFAC&redir_esc=y.

[3] P. Hofmann. *Solid State Physics: An Introduction, 2nd Edition*. Wiley-VCH, 2015. ISBN: 978-3-527-68206-5. URL: https://books.google.se/books?id=hCufzwEACAAJ.

[4] W.R. Leo. *Techniques for Nuclear and Particle Physics Experiments: A How-to Approach*. Springer, 1987. ISBN: 9783540173861. URL: https://books.google.se/books?id=hCufzwEACAAJ.

[5] E.L. Hull et al. "Temperature sensitivity of surface channel effects on high-purity germanium detectors". In: *Nuclear Instruments and Methods in Physics Research Section A: Accelerators, Spectrometers, Detectors and Associated Equipment* 364.3 (1995), pp. 488–495. ISSN: 0168-9002. DOI: https://doi.org/10.1016/0168-9002(95)00339-8. URL: https://www.sciencedirect.com/science/article/pii/0168900295003398.

[6] B. L. Wall et al. "Dead layer on silicon p-i-n diode charged-particle detectors". In: *Nuclear Instruments and Methods in Physics Research. Section A, Accelerators, Spectrometers, Detectors and Associated Equipment, 744:73-79* (Apr. 2014). DOI: 10.1016/j.nima.2013.12.048. URL: https://www.osti.gov/biblio/1132226.

[7] Philip Allport. "Applications of silicon strip and pixel-based particle tracking detectors". In: *Nature Reviews Physics* 1.9 (Sept. 2019), pp. 567–576. ISSN: 2522-5820. DOI: 10.1038/s42254-019-0081-z. URL: https://doi.org/10.1038/s42254-019-0081-z.

[8] Yonggang Wang et al. "A time-driven FPGA-based fast nuclear charge digitization method". In: *Nuclear Instruments and Methods in Physics Research Section A: Accelerators, Spectrometers, Detectors and Associated Equipment* 946 (2019), p. 162666. ISSN: 0168-9002. DOI: https://doi.org/10.1016/j.nima.2019.162666. URL: https://www.sciencedirect.com/science/article/pii/S0168900219311520.

[9] Tatsuji Matsuura. "Recent progress on CMOS successive approximation ADCs". In: *IEEJ Transactions on Electrical and Electronic Engineering* 11.5 (2016), pp. 535–548. DOI: https://doi.org/10.1002/tee.22290. eprint: https://onlinelibrary.wiley.com/doi/pdf/10.1002/tee.22290. URL: https://onlinelibrary.wiley.com/doi/abs/10.1002/tee.22290.

[10] Vahid Esmaeili-sani et al. "Neutron–gamma discrimination based on bipolar trapezoidal pulse shaping using FPGAs in NE213". In: *Nuclear Instruments and Methods in Physics Research Section A: Accelerators, Spectrometers, Detectors and Associated Equipment* 694 (2012), pp. 113–118. ISSN: 0168-9002. DOI: https://doi.org/10.1016/j.nima.2012.08.025. URL: https://www.sciencedirect.com/science/article/pii/S0168900212008935.

[11] R. Sheldon. *Arm processor*. 2022. URL: https://www.techtarget.com/whatis/definition/ARM-processor.

[12] Ametek Ortec. *A250CF CoolFET® Charge Sensitive Preamplifier - Obsolete/Discontinued after 2020*. 2023. URL: https://www.amptek.com/internal-products/obsolete-products/a250cf-coolfet-charge-sensitive-preamplifier.

[13] Ametek Ortec. *MAESTRO Multichannel Analyzer Emulation Software*. 2023. URL: https://www.ortec-online.com/products/application-software/maestro-mca.

[14] Frank Asaro, S. G. Thompson, and I. Perlman. "The Alpha Spectra of Cm^{242}, Cm^{243}, and Cm^{244}". In: *Phys. Rev.* 92 (3 Nov. 1953), pp. 694–702. DOI: 10.1103/PhysRev.92.694. URL: https://link.aps.org/doi/10.1103/PhysRev.92.694.

[15] Farghaly, Dalia. *Characterization of Double Sided Silicon Strip Detectors from LYCCA modules for FAIR*. eng. Student Paper. 2019.

[16] D. Vrtacnik et al. "Investigation of cutting edge in edge-on silicon microstrip detector". In: *Nuclear Instruments and Methods in Physics Research Section A: Accelerators, Spectrometers, Detectors and Associated Equipment* 620.2 (2010), pp. 557–562. ISSN: 0168-9002. DOI: https://doi.org/10.1016/j.nima.2010.03.144. URL: https://www.sciencedirect.com/science/article/pii/S0168900210007709.

9 Appendix

9.1 Spectra

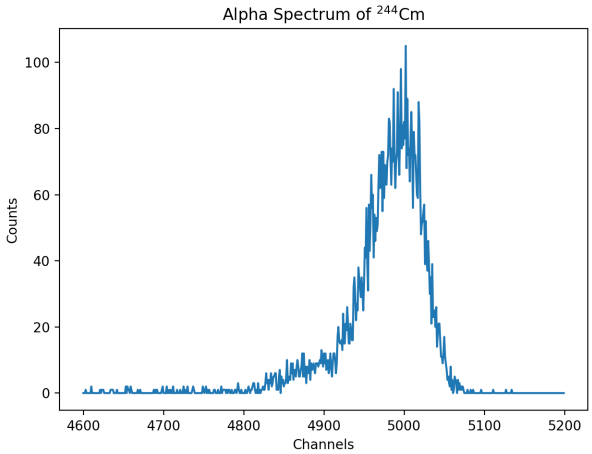

Figure 16: Figure showing alpha particle's energy spectra registered by DSSD of ^{244}Cm

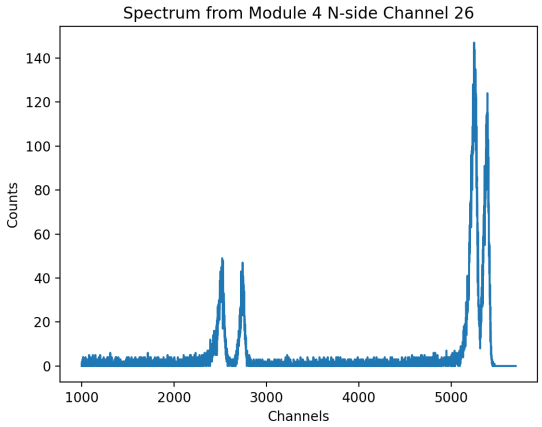

Figure 17: Figure showing the spectrum obtained from the N-side channel 26 in module 4

9.2 Hit Patterns

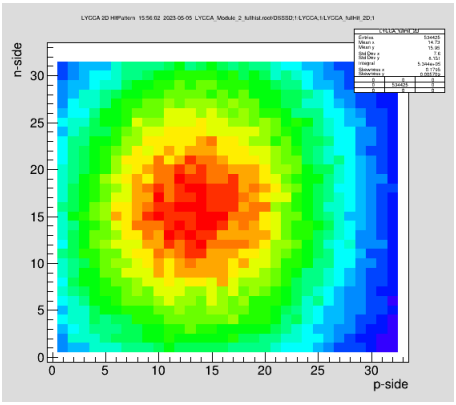

(a) PN pattern

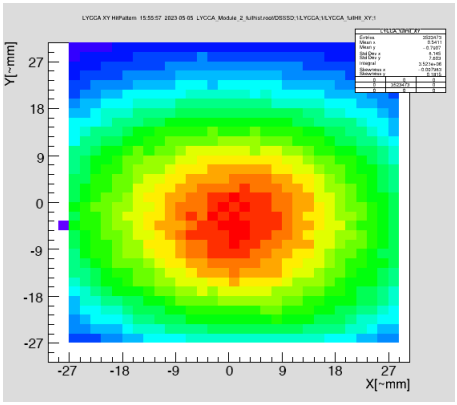

(b) XY pattern

Figure 18: Module 2 hit patterns

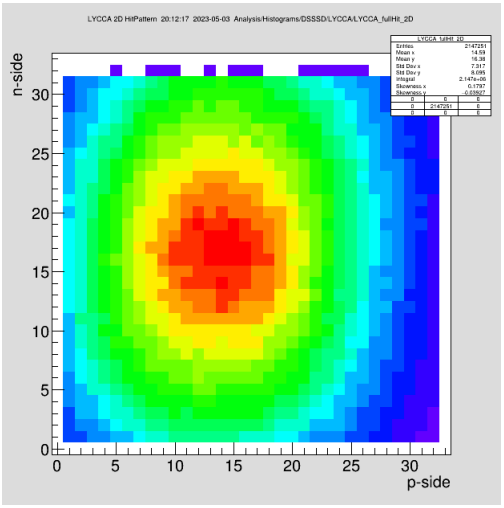

(a) PN pattern

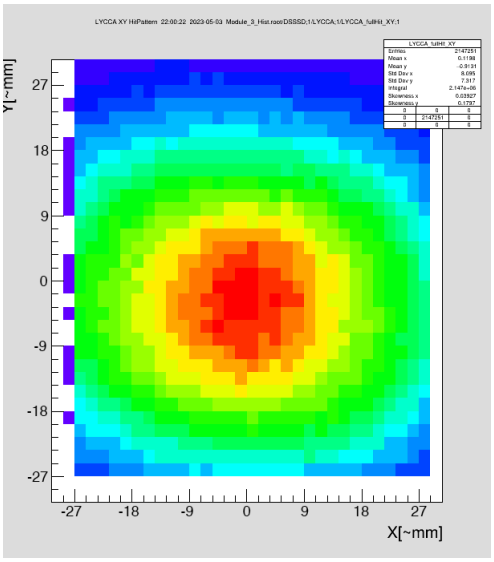

(b) XY pattern

Figure 19: Module 3 hit patterns

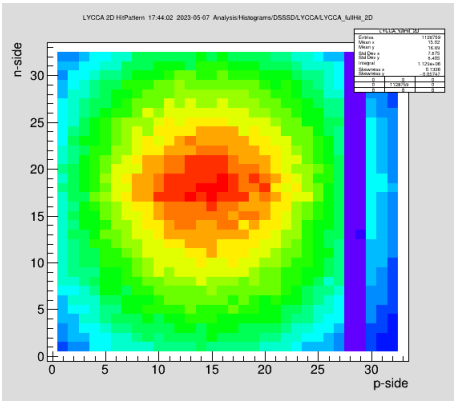

(a) PN pattern

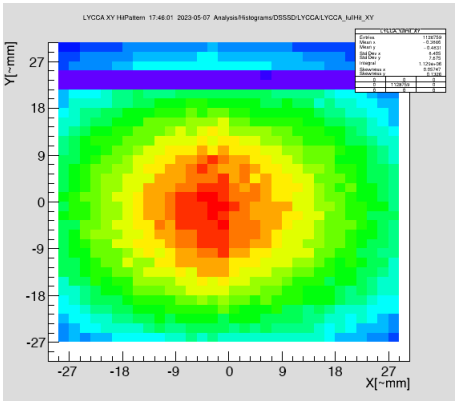

(b) XY pattern

Figure 20: Module 4 hit patterns

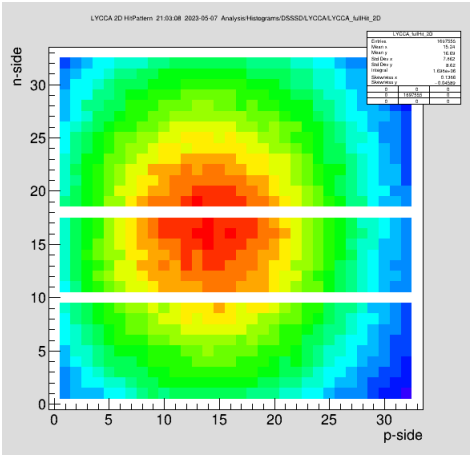

(a) PN pattern

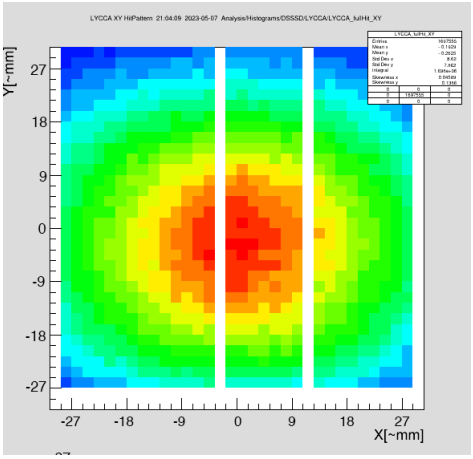

(b) XY pattern

Figure 21: Module 5 hit patterns

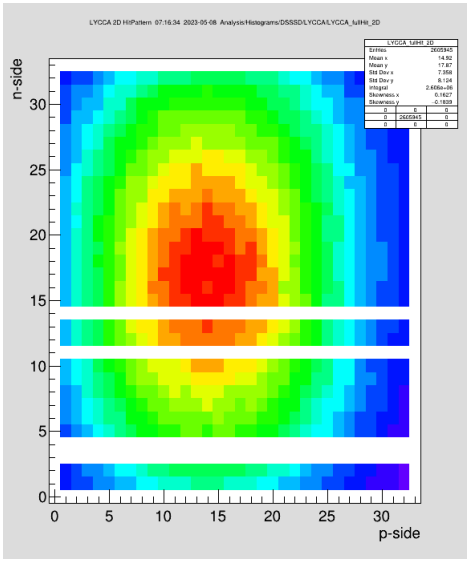

(a) PN pattern

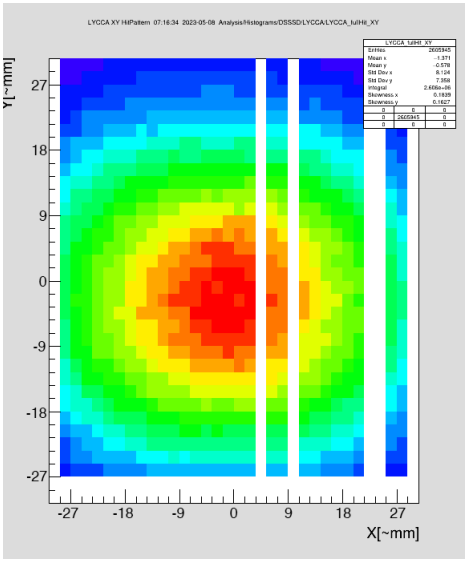

(b) XY pattern

Figure 22: Module 6 hit patterns

9.3 Resolution Graphs

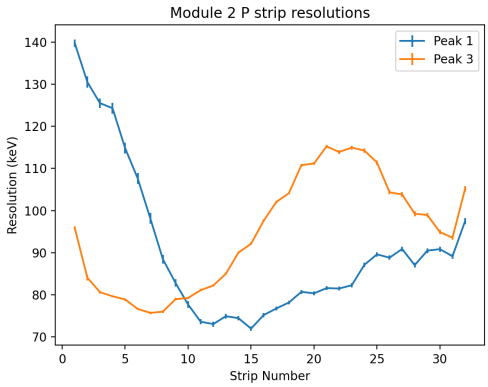

(a) P side resolution

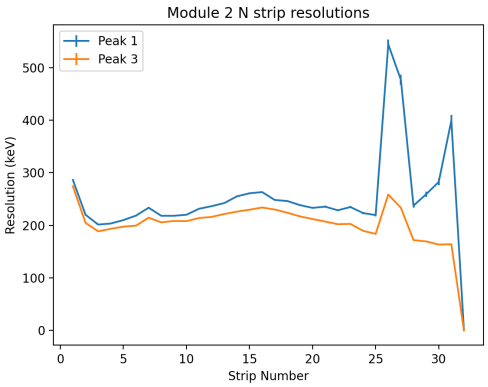

(b) N side resolution

Figure 23: Module 2 resolutions, where any resolution value of 0 indicates that the strip is malfunctioning

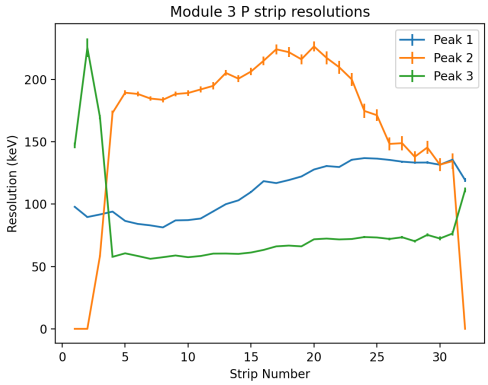

(a) P side resolution

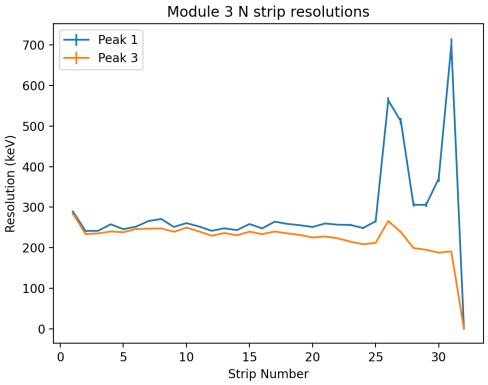

(b) N side resolution

Figure 24: Module 3 resolutions, where any resolution value of 0 indicates that the strip is malfunctioning or inability to resolve resolution

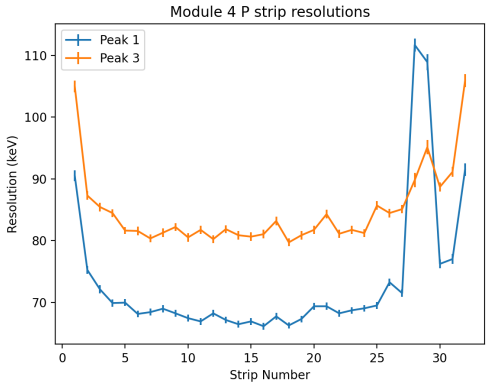

(a) P side resolution

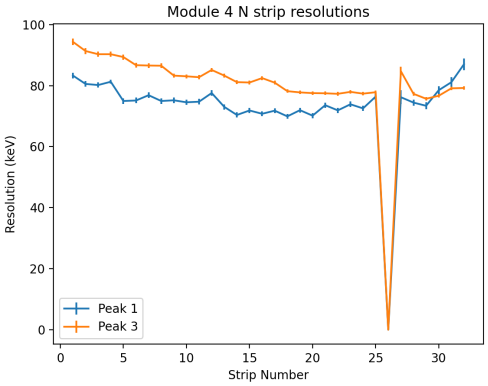

(b) N side resolution

Figure 25: Module 4 resolutions, where any resolution value of 0 indicates that the strip is malfunctioning

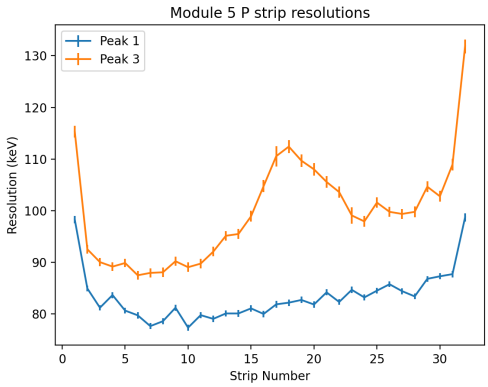

(a) P side resolution

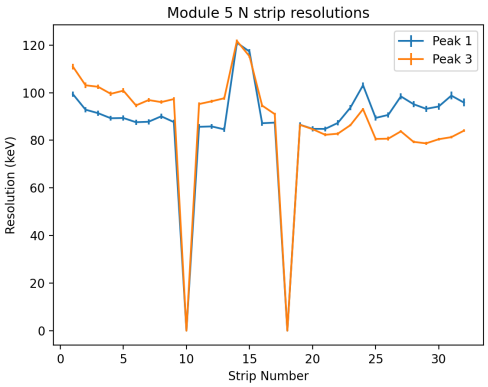

(b) N side resolution

Figure 26: Module 5 resolutions, where any resolution value of 0 indicates that the strip is malfunctioning

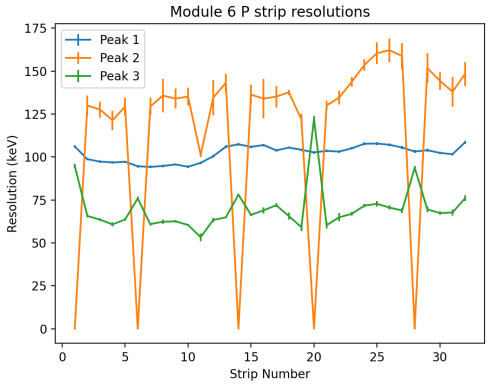

(a) P side resolution

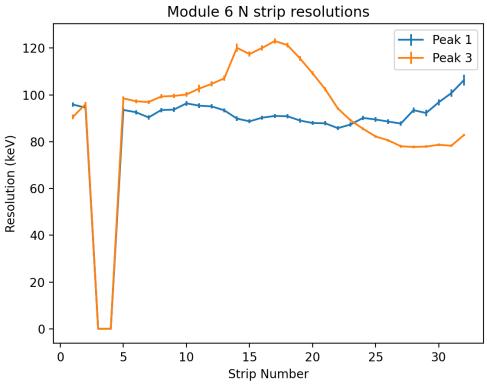

(b) N side resolution

Figure 27: Module 6 resolutions, where any resolution value of 0 indicates that the strip is malfunctioning or inability to resolve resolution

9.4 Resolution Tables

	Resolution (keV)		
Strip number	Peak 1 at 3.271 MeV	Peak 2 at 5.755 MeV	Peak 3 at 5.797 MeV
1	82.8 ± 0.7	155 ± 34	78.3 ± 2.9
2	73.4 ± 0.7	133 ± 18	70.3 ± 1.2
3	69.6 ± 0.6	128 ± 20	69.2 ± 1.6
4	69.4 ± 0.6	129 ± 16	65.4 ± 1.2
5	72.3 ± 0.7	121 ± 23	69.4 ± 2.0
6	71.1 ± 0.6	128 ± 17	68.8 ± 1.3
7	70.1 ± 0.7	123 ± 17	66.7 ± 1.6
8	69.5 ± 0.5	126 ± 29	67.4 ± 2.0
9	69.7 ± 0.7	128 ± 17	69.1 ± 1.4
10	68.0 ± 0.6	125 ± 17	66.4 ± 1.4
11	68.3 ± 0.6	128 ± 18	68.9 ± 1.4
12	67.2 ± 0.6	115 ± 29	64.3 ± 3.5
13	69.2 ± 0.7	126 ± 20	68.8 ± 1.4
14	69.7 ± 0.6	130 ± 16	68.5 ± 1.0
15	70.2 ± 0.7	126 ± 17	67.3 ± 1.3
16	66.0 ± 0.6	124 ± 13	65.8 ± 1.3
17	68.6 ± 0.6	125 ± 17	68.0 ± 1.3
18	67.7 ± 0.6	98.9 ± 2.3	58.5 ± 3.5
19	68.1 ± 0.6	117 ± 12	64.0 ± 1.7
20	69.6 ± 0.7	123 ± 17	67.0 ± 1.7
21	69.8 ± 0.7	125 ± 16	68.5 ± 1.3
22	72.9 ± 0.8	125 ± 19	70.9 ± 1.9
23	70.2 ± 0.7	128 ± 17	66.3 ± 1.6
24	68.4 ± 0.7	126 ± 14	65.7 ± 1.5
25	71.8 ± 0.7	130 ± 14	65.6 ± 1.3
26	71.4 ± 0.6	131 ± 13	66.4 ± 1.3
27	70.5 ± 0.7	129 ± 19	68.4 ± 1.5
28	71.3 ± 0.7	123 ± 14	66.5 ± 1.6
29	74.0 ± 0.7	125 ± 14	67.5 ± 1.8
30	74.5 ± 0.8	128 ± 18	68.3 ± 1.6
31	75.7 ± 0.8	132 ± 23	71.9 ± 2.3
32	91.5 ± 1.1	155 ± 23	78.3 ± 1.9

Table 4: Table for Module 1 P side.

	Resolution (keV)		
Strip number	Peak 1 at 3.271 MeV	Peak 2 at 5.755 MeV	Peak 3 at 5.797 MeV
1	85.5 ± 0.9	N/A	82.3 ± 0.8
2	82.1 ± 1.0	N/A	75.5 ± 0.7
3	81.1 ± 0.9	N/A	79.4 ± 0.7
4	78.6 ± 0.9	N/A	76.3 ± 0.6
5	80.1 ± 0.9	N/A	75.4 ± 0.6
6	79.1 ± 0.8	N/A	77.3 ± 0.6
7	78.6 ± 0.8	N/A	75.4 ± 0.6
8	80.9 ± 0.9	N/A	75.4 ± 0.6
9	81.7 ± 0.9	N/A	74.4 ± 0.6
10	81.1 ± 0.8	N/A	75.5 ± 0.5
11	77.7 ± 0.8	N/A	72.9 ± 0.5
12	78.6 ± 0.9	N/A	73.1 ± 0.5
13	78.9 ± 0.9	N/A	75.5 ± 0.6
14	77.0 ± 0.9	N/A	76.8 ± 0.5
15	79.7 ± 0.9	N/A	75.1 ± 0.5
16	78.5 ± 0.9	N/A	72.9 ± 0.5
17	77.3 ± 0.9	N/A	71.0 ± 0.5
18	82.4 ± 0.9	N/A	73.0 ± 0.5
19	78.6 ± 0.9	N/A	73.1 ± 0.5
20	78.9 ± 0.8	N/A	74.1 ± 0.5
21	80.9 ± 0.9	N/A	74.0 ± 0.5
22	77.4 ± 0.8	N/A	72.9 ± 0.5
23	79.3 ± 0.9	N/A	74.2 ± 0.5
24	80.8 ± 1.0	N/A	72.6 ± 0.5
25	81.7 ± 1.0	N/A	73.4 ± 0.6
26	81.8 ± 0.9	N/A	69.6 ± 0.5
27	81.7 ± 1.0	N/A	72.6 ± 0.5
28	82.9 ± 1.0	N/A	73.3 ± 0.5
29	N/A	N/A	N/A
30	N/A	N/A	N/A
31	87.7 ± 1.3	N/A	72.1 ± 0.5
32	94.9 ± 1.3	N/A	76.8 ± 0.5

Table 5: Table for Module 1 N side.

	Resolution (keV)		
Strip number	Peak 1 at 3.271 MeV	Peak 2 at 5.755 MeV	Peak 3 at 5.797 MeV
1	139.7 ± 0.9	N/A	95.88 ± 0.35
2	130.5 ± 1.3	N/A	84.1 ± 0.6
3	125.5 ± 1.1	N/A	80.64 ± 0.29
4	124.3 ± 1.3	N/A	79.65 ± 0.29
5	114.8 ± 1.3	N/A	78.90 ± 0.29
6	107.6 ± 1.3	N/A	76.64 ± 0.29
7	98.1 ± 1.3	N/A	75.71 ± 0.29
8	88.5 ± 1.0	N/A	76.00 ± 0.29
9	82.8 ± 0.9	N/A	78.96 ± 0.29
10	77.7 ± 0.8	N/A	79.24 ± 0.29
11	73.6 ± 0.7	N/A	81.10 ± 0.29
12	73.0 ± 0.6	N/A	82.20 ± 0.29
13	74.9 ± 0.6	N/A	84.98 ± 0.29
14	74.5 ± 0.5	N/A	90.03 ± 0.29
15	72.0 ± 0.5	N/A	92.11 ± 0.29
16	75.2 ± 0.5	N/A	97.56 ± 0.29
17	76.7 ± 0.5	N/A	102.03 ± 0.35
18	78.2 ± 0.5	N/A	104.11 ± 0.29
19	80.7 ± 0.5	N/A	110.78 ± 0.35
20	80.3 ± 0.5	N/A	111.19 ± 0.35
21	81.6 ± 0.5	N/A	115.2 ± 0.4
22	81.5 ± 0.5	N/A	113.9 ± 0.5
23	82.3 ± 0.5	N/A	115.0 ± 0.5
24	87.1 ± 0.5	N/A	114.3 ± 0.5
25	89.6 ± 0.5	N/A	111.4 ± 0.5
26	88.8 ± 0.5	N/A	104.3 ± 0.5
27	90.9 ± 0.6	N/A	103.8 ± 0.6
28	87.0 ± 0.6	N/A	99.2 ± 0.6
29	90.5 ± 0.6	N/A	99.0 ± 0.5
30	90.8 ± 0.6	N/A	94.9 ± 0.5
31	89.1 ± 0.6	N/A	93.6 ± 0.5
32	97.5 ± 0.8	N/A	105.2 ± 0.6

Table 6: Table for Module 2 P side.

	Resolution (keV)		
Strip number	Peak 1 at 3.271 MeV	Peak 2 at 5.755 MeV	Peak 3 at 5.797 MeV
1	$286.2 \pm 1.$	N/A	274.2 ± 0.8
2	$220.2 \pm 1.$	N/A	204.7 ± 0.7
3	$201.5 \pm 1.$	N/A	188.6 ± 0.7
4	$203.5 \pm 1.$	N/A	193.4 ± 0.6
5	$210.0 \pm 1.$	N/A	197.6 ± 0.6
6	$218.5 \pm 1.$	N/A	199.4 ± 0.6
7	$233.6 \pm 1.$	N/A	214.5 ± 0.6
8	$218.2 \pm 1.$	N/A	205.7 ± 0.6
9	$218.2 \pm 1.$	N/A	208.3 ± 0.6
10	$220.2 \pm 1.$	N/A	208.0 ± 0.5
11	$231.6 \pm 1.$	N/A	213.9 ± 0.5
12	$236.5 \pm 1.$	N/A	216.1 ± 0.5
13	$242.4 \pm 1.$	N/A	221.6 ± 0.6
14	$255.2 \pm 1.$	N/A	226.1 ± 0.5
15	$261.0 \pm 1.$	N/A	229.7 ± 0.5
16	$263.3 \pm 1.$	N/A	234.0 ± 0.5
17	$248.3 \pm 1.$	N/A	230.1 ± 0.5
18	$246.3 \pm 1.$	N/A	224.0 ± 0.5
19	$238.5 \pm 1.$	N/A	217.1 ± 0.5
20	$233.2 \pm 1.$	N/A	212.0 ± 0.5
21	$235.5 \pm 2.$	N/A	207.2 ± 0.5
22	$228.7 \pm 2.$	N/A	202.2 ± 0.5
23	$234.9 \pm 2.$	N/A	202.8 ± 0.5
24	$223.4 \pm 2.$	N/A	189.6 ± 0.5
25	$219.5 \pm 2.$	N/A	183.8 ± 0.6
26	545 ± 9	N/A	258.7 ± 0.5
27	477 ± 9	N/A	233.4 ± 0.5
28	237 ± 4	N/A	171.9 ± 0.5
29	259 ± 5	N/A	169.4 ± 0.5
30	283 ± 7	N/A	163.4 ± 0.5
31	399 ± 10	N/A	164.1 ± 0.5
32	N/A	N/A	N/A

Table 7: Table for Module 2 N side.

	Resolution (keV)		
Strip number	Peak 1 at 3.271 MeV	Peak 2 at 5.755 MeV	Peak 3 at 5.797 MeV
1	97.8 ± 0.6	N/A	$147.2 \pm 2.$
2	89.7 ± 0.7	N/A	226 ± 8
3	91.7 ± 0.5	58.4 ± 0.6	169.9 ± 1.6
4	94.0 ± 0.4	173.2 ± 1.7	57.7 ± 0.5
5	86.6 ± 0.4	189.4 ± 1.8	60.6 ± 0.5
6	84.2 ± 0.4	188.4 ± 1.8	58.4 ± 0.4
7	83.0 ± 0.4	184.7 ± 1.7	56.17 ± 0.35
8	81.4 ± 0.4	183.7 ± 2.0	57.4 ± 0.4
9	87.0 ± 0.5	188.4 ± 2.0	58.8 ± 0.4
10	87.2 ± 0.5	189.2 ± 2.3	57.4 ± 0.4
11	88.5 ± 0.5	192.1 ± 2.3	58.43 ± 0.35
12	94.2 ± 0.5	194.9 ± 2.9	60.3 ± 0.4
13	100.0 ± 0.5	205.3 ± 2.3	60.40 ± 0.29
14	103.1 ± 0.6	200.7 ± 2.9	60.11 ± 0.35
15	109.8 ± 0.7	206.4 ± 2.9	61.22 ± 0.35
16	118.5 ± 0.6	215.1 ± 3.4	63.30 ± 0.35
17	116.9 ± 0.5	224 ± 4	66.1 ± 0.4
18	119.3 ± 0.5	222 ± 4	66.8 ± 0.4
19	122.2 ± 0.5	216 ± 4	66.1 ± 0.4
20	127.8 ± 0.5	227 ± 4	71.8 ± 0.4
21	130.6 ± 0.6	217 ± 5	72.4 ± 0.5
22	129.8 ± 0.7	210 ± 5	71.7 ± 0.5
23	135.6 ± 0.7	200 ± 5	72.1 ± 0.6
24	136.9 ± 0.8	175 ± 6	73.6 ± 0.7
25	136.5 ± 0.8	171 ± 5	73.3 ± 0.6
26	135.5 ± 0.8	148 ± 5	72.1 ± 0.9
27	134.1 ± 0.9	149 ± 6	73.4 ± 1.0
28	133.4 ± 0.9	138 ± 5	70.3 ± 1.2
29	133.4 ± 0.9	145 ± 5	75.4 ± 1.2
30	131.6 ± 0.9	132 ± 5	72.5 ± 1.5
31	135.7 ± 1.1	135 ± 6	76.5 ± 1.8
32	119.4 ± 1.6	N/A	111.4 ± 1.8

Table 8: Table for Module 3 P side.

	Resolution (keV)		
Strip number	Peak 1 at 3.271 MeV	Peak 2 at 5.755 MeV	Peak 3 at 5.797 MeV
1	289.2 ± 1.6	N/A	285 ± 4
2	241.1 ± 1.6	N/A	233.6 ± 2.3
3	241.7 ± 1.3	N/A	235.4 ± 2.0
4	257.8 ± 1.3	N/A	240.0 ± 1.9
5	245.7 ± 1.3	N/A	238.2 ± 1.8
6	251.9 ± 1.3	N/A	246.1 ± 1.4
7	266.0 ± 1.6	N/A	247.0 ± 1.4
8	270.9 ± 1.6	N/A	247.5 ± 1.4
9	251.2 ± 1.3	N/A	239.3 ± 1.2
10	260.7 ± 1.3	N/A	249.5 ± 1.0
11	252.2 ± 1.3	N/A	240.1 ± 1.2
12	241.7 ± 1.3	N/A	229.4 ± 1.0
13	248.0 ± 1.3	N/A	236.3 ± 1.0
14	243.4 ± 1.3	N/A	230.6 ± 0.9
15	258.4 ± 1.6	N/A	239.7 ± 1.0
16	247.6 ± 1.6	N/A	233.4 ± 1.0
17	264.3 ± 1.6	N/A	240.1 ± 0.9
18	258.8 ± 1.6	N/A	235.4 ± 0.9
19	255.5 ± 1.6	N/A	231.5 ± 0.9
20	251.2 ± 2.0	N/A	225.3 ± 0.8
21	259.7 ± 2.0	N/A	227.6 ± 0.8
22	256.8 ± 2.3	N/A	223.2 ± 0.8
23	256.1 ± 2.3	N/A	215.0 ± 0.8
24	248.6 ± 2.6	N/A	208.6 ± 0.8
25	265.3 ± 2.9	N/A	212.0 ± 0.8
26	563 ± 8	N/A	265.8 ± 0.9
27	512 ± 8	N/A	238.5 ± 0.8
28	306 ± 5	N/A	199.2 ± 0.7
29	306 ± 6	N/A	194.9 ± 0.7
30	371 ± 8	N/A	187.9 ± 0.6
31	700 ± 16	N/A	190.8 ± 0.7
32	N/A	N/A	N/A

Table 9: Table for Module 3 N side.

	Resolution (keV)		
Strip number	Peak 1 at 3.271 MeV	Peak 2 at 5.755 MeV	Peak 3 at 5.797 MeV
1	90.5 ± 0.9	N/A	105.0 ± 0.9
2	75.2 ± 0.7	N/A	87.3 ± 0.7
3	72.1 ± 0.7	N/A	85.4 ± 0.7
4	69.9 ± 0.6	N/A	84.5 ± 0.6
5	69.9 ± 0.6	N/A	81.6 ± 0.6
6	68.1 ± 0.6	N/A	81.6 ± 0.7
7	68.4 ± 0.6	N/A	80.3 ± 0.6
8	69.0 ± 0.6	N/A	81.3 ± 0.7
9	68.2 ± 0.6	N/A	82.2 ± 0.6
10	67.4 ± 0.6	N/A	80.5 ± 0.7
11	66.9 ± 0.6	N/A	81.7 ± 0.7
12	68.2 ± 0.6	N/A	80.2 ± 0.6
13	67.1 ± 0.6	N/A	81.9 ± 0.6
14	66.4 ± 0.6	N/A	80.9 ± 0.7
15	66.9 ± 0.6	N/A	80.6 ± 0.7
16	66.1 ± 0.6	N/A	81.0 ± 0.7
17	67.7 ± 0.6	N/A	83.2 ± 0.7
18	66.2 ± 0.5	N/A	79.7 ± 0.6
19	67.3 ± 0.5	N/A	80.9 ± 0.7
20	69.4 ± 0.6	N/A	81.7 ± 0.7
21	69.4 ± 0.6	N/A	84.3 ± 0.7
22	68.2 ± 0.6	N/A	81.1 ± 0.6
23	68.7 ± 0.5	N/A	81.7 ± 0.7
24	69.0 ± 0.6	N/A	81.2 ± 0.6
25	69.5 ± 0.6	N/A	85.7 ± 0.7
26	73.2 ± 0.6	N/A	84.5 ± 0.7
27	71.5 ± 0.6	N/A	85.1 ± 0.7
28	111.7 ± 1.0	N/A	89.8 ± 1.2
29	108.9 ± 1.3	N/A	95.1 ± 1.2
30	76.2 ± 0.7	N/A	88.7 ± 0.8
31	77.0 ± 0.8	N/A	91.1 ± 0.8
32	91.5 ± 1.0	N/A	105.9 ± 1.0

Table 10: Table for Module 4 P side.

	Resolution (keV)		
Strip number	Peak 1 at 3.271 MeV	Peak 2 at 5.755 MeV	Peak 3 at 5.797 MeV
1	83.3 ± 0.9	N/A	94.4 ± 1.1
2	80.6 ± 0.9	N/A	91.4 ± 1.0
3	80.2 ± 0.9	N/A	90.3 ± 0.9
4	81.3 ± 0.7	N/A	90.3 ± 0.9
5	75.0 ± 0.9	N/A	89.4 ± 0.9
6	75.1 ± 0.9	N/A	86.7 ± 0.8
7	76.9 ± 0.9	N/A	86.6 ± 0.8
8	75.0 ± 0.9	N/A	86.5 ± 0.8
9	75.2 ± 0.9	N/A	83.3 ± 0.7
10	74.6 ± 0.9	N/A	83.1 ± 0.6
11	74.7 ± 0.9	N/A	82.8 ± 0.7
12	77.6 ± 0.9	N/A	85.2 ± 0.7
13	73.0 ± 0.9	N/A	83.3 ± 0.6
14	70.4 ± 0.9	N/A	81.2 ± 0.6
15	71.9 ± 0.9	N/A	81.0 ± 0.6
16	70.8 ± 0.8	N/A	82.5 ± 0.6
17	71.8 ± 0.8	N/A	81.0 ± 0.6
18	69.9 ± 0.8	N/A	78.2 ± 0.6
19	72.0 ± 0.8	N/A	77.8 ± 0.6
20	70.2 ± 0.8	N/A	77.6 ± 0.6
21	73.6 ± 0.9	N/A	77.5 ± 0.6
22	71.9 ± 0.9	N/A	77.3 ± 0.6
23	73.9 ± 0.9	N/A	78.0 ± 0.5
24	72.6 ± 0.9	N/A	77.4 ± 0.6
25	76.4 ± 1.0	N/A	77.9 ± 0.6
26	Double Peaked	N/A	Double Peaked
27	76.2 ± 2.3	N/A	84.8 ± 1.4
28	74.5 ± 1.0	N/A	77.3 ± 0.6
29	73.4 ± 1.1	N/A	75.7 ± 0.6
30	78.5 ± 1.3	N/A	76.7 ± 0.5
31	81.1 ± 1.6	N/A	79.1 ± 0.5
32	87.0 ± 2.0	N/A	79.2 ± 0.6

Table 11: Table for Module 4 N side.

	Resolution (keV)		
Strip number	Peak 1 at 3.271 MeV	Peak 2 at 5.755 MeV	Peak 3 at 5.797 MeV
1	98.3 ± 0.7	N/A	115.3 ± 1.1
2	84.9 ± 0.5	N/A	92.5 ± 0.8
3	81.2 ± 0.5	N/A	90.0 ± 0.8
4	83.6 ± 0.6	N/A	89.2 ± 0.9
5	80.6 ± 0.5	N/A	89.9 ± 0.8
6	79.7 ± 0.6	N/A	87.5 ± 0.9
7	77.6 ± 0.6	N/A	87.9 ± 0.9
8	78.6 ± 0.6	N/A	88.1 ± 0.9
9	81.2 ± 0.6	N/A	90.2 ± 0.9
10	77.3 ± 0.6	N/A	89.0 ± 0.9
11	79.8 ± 0.6	N/A	89.7 ± 0.9
12	79.0 ± 0.6	N/A	92.1 ± 0.9
13	80.1 ± 0.6	N/A	95.1 ± 0.9
14	80.1 ± 0.7	N/A	95.5 ± 1.0
15	81.1 ± 0.7	N/A	98.9 ± 1.0
16	80.0 ± 0.6	N/A	104.8 ± 1.2
17	81.8 ± 0.7	N/A	110.5 ± 2.0
18	82.2 ± 0.6	N/A	112.4 ± 1.3
19	82.7 ± 0.6	N/A	109.7 ± 1.2
20	81.8 ± 0.6	N/A	108.0 ± 1.2
21	84.2 ± 0.6	N/A	105.6 ± 1.1
22	82.3 ± 0.6	N/A	103.6 ± 1.1
23	84.7 ± 0.6	N/A	99.1 ± 1.6
24	83.2 ± 0.6	N/A	97.9 ± 1.0
25	84.5 ± 0.5	N/A	101.6 ± 1.0
26	85.7 ± 0.5	N/A	99.8 ± 1.0
27	84.4 ± 0.6	N/A	99.4 ± 1.0
28	83.4 ± 0.5	N/A	99.8 ± 1.0
29	86.8 ± 0.6	N/A	104.6 ± 1.0
30	87.3 ± 0.6	N/A	102.8 ± 1.0
31	87.7 ± 0.6	N/A	108.9 ± 1.2
32	98.7 ± 0.8	N/A	131.8 ± 1.3

Table 12: Table for Module 5 P side.

	Resolution (keV)		
Strip number	Peak 1 at 3.271 MeV	Peak 2 at 5.755 MeV	Peak 3 at 5.797 MeV
1	99.4 ± 1.1	N/A	111.0 ± 1.2
2	92.9 ± 1.1	N/A	103.1 ± 1.2
3	91.4 ± 1.1	N/A	102.5 ± 1.0
4	89.3 ± 1.1	N/A	99.5 ± 0.9
5	89.4 ± 1.1	N/A	100.9 ± 1.0
6	87.6 ± 1.1	N/A	94.7 ± 0.8
7	87.8 ± 1.1	N/A	96.9 ± 0.9
8	90.1 ± 1.1	N/A	96.1 ± 0.8
9	87.7 ± 1.0	N/A	97.3 ± 0.7
10	N/A	N/A	N/A
11	85.7 ± 1.1	N/A	95.2 ± 0.7
12	85.8 ± 1.0	N/A	96.4 ± 0.6
13	84.6 ± 1.0	N/A	97.7 ± 0.6
14	121.0 ± 1.3	N/A	121.7 ± 0.6
15	117.3 ± 1.1	N/A	115.3 ± 0.6
16	87.2 ± 1.0	N/A	94.6 ± 0.6
17	87.4 ± 1.0	N/A	91.0 ± 0.6
18	N/A	N/A	N/A
19	86.6 ± 1.0	N/A	86.5 ± 0.6
20	84.8 ± 1.0	N/A	84.7 ± 0.6
21	84.8 ± 1.0	N/A	82.3 ± 0.6
22	87.3 ± 1.1	N/A	82.8 ± 0.6
23	93.8 ± 1.0	N/A	86.4 ± 0.5
24	103.1 ± 1.1	N/A	93.1 ± 0.5
25	89.4 ± 1.1	N/A	80.6 ± 0.6
26	90.7 ± 1.1	N/A	80.7 ± 0.9
27	98.5 ± 1.3	N/A	83.8 ± 0.5
28	95.2 ± 1.3	N/A	79.4 ± 0.6
29	93.2 ± 1.3	N/A	78.7 ± 0.6
30	94.2 ± 1.3	N/A	80.5 ± 0.6
31	98.8 ± 1.6	N/A	81.3 ± 0.5
32	95.8 ± 1.6	N/A	84.1 ± 0.5

Table 13: Table for Module 5 N side.

	Resolution (keV)		
Strip number	Peak 1 at 3.271 MeV	Peak 2 at 5.755 MeV	Peak 3 at 5.797 MeV
1	106.1 ± 0.8	N/A	94.8 ± 1.2
2	98.7 ± 0.7	130 ± 6	65.7 ± 0.9
3	97.3 ± 0.7	128 ± 5	63.5 ± 0.8
4	96.8 ± 0.8	121 ± 6	60.8 ± 1.2
5	97.2 ± 0.7	129 ± 5	63.7 ± 0.8
6	94.6 ± 0.7	N/A	75.9 ± 1.0
7	94.2 ± 0.7	129 ± 5	60.9 ± 0.8
8	94.8 ± 0.8	136 ± 10	62.3 ± 1.2
9	95.7 ± 0.7	134 ± 6	62.5 ± 0.8
10	94.3 ± 0.8	135 ± 5	60.4 ± 0.6
11	96.6 ± 0.8	101.3 ± 1.4	53.3 ± 2.3
12	100.4 ± 0.9	135 ± 10	63.4 ± 1.3
13	106.0 ± 0.8	143 ± 5	64.9 ± 0.6
14	107.4 ± 0.9	N/A	78.1 ± 0.7
15	105.9 ± 0.8	136 ± 6	66.3 ± 0.8
16	106.9 ± 0.8	134 ± 12	68.9 ± 1.8
17	103.8 ± 0.7	135 ± 6	71.9 ± 1.2
18	105.5 ± 0.7	137.7 ± 1.5	65.6 ± 2.0
19	104.2 ± 0.8	121.9 ± 3.4	59.1 ± 2.3
20	102.7 ± 0.8	N/A	122.2 ± 1.8
21	103.5 ± 0.8	129.9 ± 2.9	60.3 ± 2.0
22	103.1 ± 0.8	135 ± 4	64.9 ± 2.3
23	105.0 ± 0.8	143.8 ± 2.9	66.9 ± 1.2
24	107.7 ± 0.8	153.5 ± 3.4	71.7 ± 1.0
25	107.8 ± 0.9	160 ± 6	72.8 ± 1.6
26	107.1 ± 0.8	162 ± 7	70.5 ± 1.3
27	105.5 ± 0.8	159 ± 7	68.9 ± 1.4
28	103.2 ± 0.8	N/A	93.7 ± 1.0
29	103.9 ± 0.9	152 ± 9	69.6 ± 1.6
30	102.4 ± 0.8	144 ± 5	67.4 ± 1.0
31	101.6 ± 0.8	138 ± 9	67.7 ± 1.8
32	108.5 ± 0.9	148 ± 7	75.9 ± 1.6

Table 14: Table for Module 6 P side.

	Resolution (keV)		
Strip number	Peak 1 at 3.271 MeV	Peak 2 at 5.755 MeV	Peak 3 at 5.797 MeV
1	95.9 ± 0.9	N/A	90.5 ± 1.0
2	94.5 ± 0.9	N/A	96.1 ± 0.9
3	N/A	N/A	N/A
4	N/A	N/A	N/A
5	93.6 ± 0.9	N/A	98.5 ± 0.8
6	92.6 ± 0.9	N/A	97.3 ± 0.8
7	90.4 ± 0.9	N/A	96.9 ± 0.9
8	93.5 ± 0.9	N/A	99.3 ± 0.9
9	93.7 ± 1.0	N/A	99.5 ± 1.0
10	96.4 ± 1.0	N/A	100.2 ± 1.0
11	95.4 ± 1.0	N/A	102.7 ± 1.7
12	95.1 ± 0.9	N/A	104.7 ± 1.1
13	93.4 ± 0.9	N/A	107.1 ± 1.1
14	89.9 ± 1.0	N/A	120.1 ± 1.8
15	88.7 ± 0.8	N/A	117.4 ± 1.2
16	90.3 ± 0.8	N/A	120.1 ± 1.2
17	91.0 ± 0.9	N/A	123.0 ± 1.2
18	90.9 ± 0.9	N/A	121.3 ± 1.0
19	89.0 ± 0.9	N/A	115.6 ± 1.0
20	88.0 ± 0.9	N/A	109.2 ± 0.8
21	87.9 ± 0.9	N/A	102.4 ± 0.8
22	85.8 ± 0.9	N/A	94.2 ± 0.6
23	87.3 ± 0.9	N/A	89.2 ± 0.6
24	90.2 ± 1.0	N/A	85.5 ± 0.6
25	89.5 ± 1.0	N/A	82.2 ± 0.6
26	88.6 ± 1.0	N/A	80.6 ± 0.6
27	87.7 ± 1.0	N/A	78.0 ± 0.6
28	93.5 ± 1.1	N/A	77.7 ± 0.5
29	92.3 ± 1.3	N/A	77.9 ± 0.6
30	96.8 ± 1.3	N/A	78.7 ± 0.6
31	100.8 ± 1.6	N/A	78.3 ± 0.5
32	106.3 ± 2.3	N/A	82.8 ± 0.5

Table 15: Table for Module 6 N side.